Locally synchronized ciliary domains and tissue-scale cilia alignment underlie global metachronal wave patterns

Christa Ringers[1,2], Stephan Bialonski[3,4], Anton Solovev[4,5], Jan N. Hansen[2], Mert Ege[1], Benjamin M. Friedrich[4,5,#], and Nathalie Jurisch-Yaksi[1,2,#]

[1]*Department of Clinical and Molecular Medicine, NTNU, Trondheim, Norway,* [2]*Kavli Institute for Systems Neuroscience and Centre for Neural Computation, NTNU, Trondheim, Norway,* [3]*Institute for data-driven technologies, Aachen University of Applied Sciences, 52428 Jülich, Germany,* [4]*Center for Advancing Electronics Dresden (cfaed), Technical University Dresden, D-01062 Dresden, Germany,* [5] *Cluster of Excellence 'Physics of Life', Technical University Dresden, Arnoldstraße 18, 01307 Dresden, Germany*

[#]Authors for correspondence: nathalie.jurisch-yaksi@ntnu.no, and benjamin.m.friedrich@tu-dresden.de

ABSTRACT

Motile cilia are hair-like cell extensions present in multiple organs of the body. How cilia coordinate their regular beat in multiciliated epithelia to move fluids remains insufficiently understood, particularly due to lack of rigorous quantification. We combine here experiments, novel analysis tools, and theory to address this knowledge gap. We investigate collective dynamics of cilia in the zebrafish nose, due to its conserved properties with other ciliated tissues and its superior accessibility for non-invasive imaging. We revealed that cilia are synchronized only locally and that the size of local synchronization domains increases with the viscosity of the surrounding medium. Despite the fact that synchronization is local only, we observed global patterns of traveling metachronal waves across the multiciliated epithelium. Intriguingly, these global wave direction patterns are conserved across individual fish, but different for left and right nose, unveiling a chiral asymmetry of metachronal coordination. To understand the implications of synchronization for fluid pumping, we used a computational model of a regular array of cilia. We found that local metachronal synchronization prevents steric collisions and improves fluid pumping in dense cilia carpets, but hardly affects the direction of fluid flow. In conclusion, we show that local synchronization together with tissue-scale cilia alignment are sufficient to generate metachronal wave patterns in multiciliated epithelia, which enhance their physiological function of fluid pumping.

INTRODUCTION

Motile cilia are highly conserved, hair-like cell appendages that beat periodically to move fluid in a wide range of species. In vertebrates, motile cilia are present in the brain, the respiratory system, reproductive tracts, and the left-right organizer, where they serve numerous functions related to fluid transport. Cilia move cerebrospinal fluid along the ventricles of the vertebrate brain [1, 2, 3, 4, 5, 6] and spinal cord [7, 8], contribute to mucociliary clearance, which protect our lungs and nose from pathogens [9, 10, 11], or establish the left-right body axis during embryonic development [12, 13]. Cilia often coordinate their movements within and across cell boundaries [14, 15, 16, 17], which may improve cilia-mediated fluid transport as suggested by modeling studies [18]. Yet, how cilia coordination emerges in multiciliated tissues remains an active topic of research.

In the absence of a tissue-scale ciliary pacemaker, cilia require a physical coupling to coordinate their beat. Coupling between cilia can occur through the surrounding fluid, which is referred to as hydrodynamic coupling, as originally proposed by Taylor [19] and first demonstrated experimentally for pairs of cilia [20]. In short, the movement of one cilium sets the surrounding fluid in motion, which impacts hydrodynamic friction forces on other cilia in its vicinity. A change in hydrodynamic friction forces causes cilia to beat slightly faster or slower [21]. Theoretical studies showed that hydrodynamic interactions could, at least in principle, orchestrate self-organized synchronization of cilia in a traveling wave of cilia phase, known as metachronal waves [18, 22, 23, 24, 25, 26, 27, 28]. Additionally, basal coupling of cilia through their anchoring in the cell cortex may contribute to cilia synchronization [29, 30, 31, 32]. Putative synchronization mechanisms must be sufficiently strong to overcome the deleterious effects of slightly distinct beat frequencies, active cilia noise [33, 34, 35, 36], and disorder in cilia alignment [37]. Hence, global synchronization across an entire tissue is rather unlikely.

The localization of cilia carpets deep inside the vertebrate body has motivated previous studies of cilia carpet dynamics to resort to more accessible and simpler, non-animal model systems on the surface of protists such as *Paramecium* [16] or the green alga *Volvox* [15, 16], or cell culture systems [38, 39, 40, 41]. Intriguingly, cilia coordination in the form of metachronal waves is observed in some systems, but not in others, prompting the open question on the determinants of cilia synchronization. Previous work showed that cilia density and spatial distribution [38, 41], the viscosity of the surrounding fluid (e.g., mucus versus water [16]), as well as the tissue-scale alignment of cilia polarity [42] appear to be key parameters for synchronization in cilia carpets. Intriguingly, the

wave direction of these metachronal waves can be rotated relative to the direction of the effective stroke of the cilia beat [17]. This broken chiral symmetry of metachronal waves is likely a consequence of chiral cilia beat patterns [18, 26, 27], but the details are not understood. Finally, it is not even clear to what extent metachronal coordination is rather a local or a tissue-scale phenomenon, and how this in turn affects the pumping rate of cilia carpets. Answering these open questions requires accessible model systems.

In this study, we combined experimental and theoretical work to study the coordination of motile cilia and its impact on fluid pumping. We chose as experimental model the larval zebrafish nose, which is a cup-like structure of circa 50 µm diameter containing many multiciliated cells [43], which allows for non-invasive biophysical measurements of cilia beating due to its superficial location. Using this *in vivo* model, we observed that the cilia beat frequency is heterogeneous across the epithelium, limiting synchronization to local domains. Notwithstanding, we identified robust metachronal coordination, with waves that propagated along stable directions across the multiciliated epithelium. The direction of metachronal waves is rotated by approximately 90° in the right nose as compared to the left nose. This difference between left and right nose marks an instance of broken chiral symmetry, which is not explained by cilia orientation. To understand the implications for fluid pumping of local synchronization as observed in the zebrafish nose, we used a computational model of a regular array of cilia [27, 36]. We detail how local synchronization is necessary to avoid steric collisions between cilia at higher cilia densities, which helps efficient cilia beating. At the same time, the rate of fluid pumping is robust against weak levels of noise. Finally, we showed that the direction and wavelength of metachronal traveling waves influence the mean pumping rate, but hardly affects the direction of fluid flow.

Altogether, we propose that local synchronization together with tissue-scale cilia alignment is sufficient for the emergence of global metachronal waves in a cilia carpet, which in turn support its physiological function of fluid pumping.

RESULTS

The dense packing of multiciliated cells in the zebrafish nose provides a powerful model to study cilia coordination

To study how cilia beating coordinates throughout an entire ciliated organ in its native state, we turned to the larval zebrafish nose, as its localization on the snout allows for non-invasive live imaging of an entire tissue (Fig. 1A & Suppl. 1A). At four-days post fertilization, the zebrafish nose is a cup-like structure containing multiciliated cells at its rim and olfactory sensory neurons and support cells in its center [43, 44, 45]. To characterize the three-dimensional organization of motile cilia in this organ, we quantified the number, distribution, and properties of multiciliated cells. We imaged four-day old larvae that expressed a GFP-based indicator within multiciliated cells (*Tg(Foxj1a:GCaMP6s)*), and that were stained for the ciliary markers, acetylated tubulin [43] and glutamylated tubulin [1, 46](Fig. 1B & Suppl. 1B). Our results revealed that the distribution of multiciliated cells across the 3D geometry of the nose is stereotypical: most cells populate the lateral rim, forming two to three rows of multiciliated cells, while fewer cells occupy the medial rim, and are even absent in the anteromedial center regions (Fig. 1B&C). This pattern is highly consistent

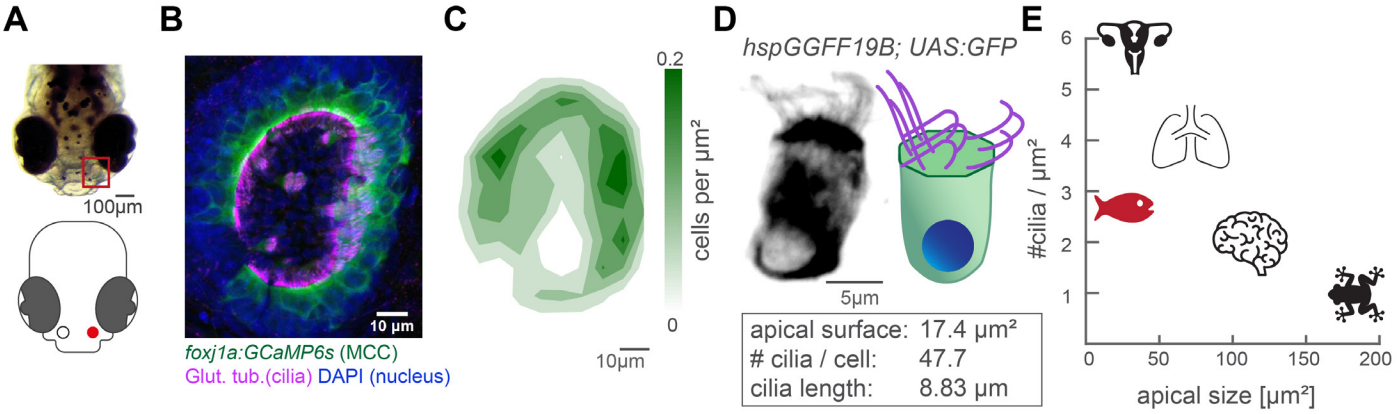

FIGURE 1: The zebrafish nose as model system for a ciliated epithelium with small and densely packed multiciliated cells.*(A) A 4-day old zebrafish larva (top) and its schematic drawing (bottom). (B) A representative example of a left nose marked by a red box in (A). In the maximum projection, motile cilia are labelled in magenta (glutamylated tubulin), nuclei in blue (DAPI), and multiciliated cells in green (foxj1a:GCaMP6s). Note the lack of multiciliated cells in the center of the nose. DAPI signals highlight the presence of other cell types. (C) A contour plot showing the average multiciliated cell density (maximum projection) with a total number of 50.8 multiciliated cells per fish (± 6.24 SD; n = 15). (D) A representative example (left) and schematic (right) of a multiciliated cell. On average, each cell has 47.7 cilia (± 9.94 SD; n = 4), the apical surface spans 17.4 µm² (± 6.3 SD; n = 11), and cilia are 8.83 µm long (± 0.86 SD; n = 38; Suppl. 1B-D'). (E) A graph depicting ciliary density per cell across animals and organs. Shown are the zebrafish nose, clawed frog skin (47, 48), mouse brain ventricles (49), lungs (46), and oviduct (50). All n refer to the number of fish. SD = standard deviation.*

across fish and mirrored for left and right noses (Supp. 1B). We identified that on average each nose contains 50.8 multiciliated cells (± 6.24; Suppl. 1B-B'). We also measured that 47.7 cilia (± 9.94; Suppl. 1C-C') emanate from an apical cell surface of 17.4 μm^2 (± 6.31; Suppl. 1D-D'), with a length of 8.8µm (± 0.86; Suppl. 1E-E'). From the abovementioned values, we calculated the distance between cilia to be 0.68 µm, and a cellular density of 2.74 cilia/μm^2. Altogether, our results revealed that multiciliated cells in the four-day old zebrafish nose contain fewer cilia than multiciliated cells of the lung epithelium (>100 cilia per cell)[47] or *Xenopus laevis* embryonic skin (~150 cilia per cell)[48, 49], but retain a similar cilia density due to their reduced apical surface (Fig. 1E). Because of this, we argue that the larval zebrafish nose is a powerful model to study cilia coordination within and across neighboring cells in a three-dimensional multiciliated carpet.

Frequency heterogeneity restricts the synchronization of cilia to a local scale

To understand the dynamic properties of cilia beating in our system and their impact on ciliary coordination, we recorded cilia beating with light transmission microscopy and measured the ciliary beat frequency (CBF) using an FFT-based method (Fig. 2A-C and Methods) adapted from [43]. Using this technique, we observed that CBF is heterogenous in the nose but organized in frequency patches (Fig. 2C & Suppl. 2A). This CBF map remained stable over time (Suppl. 2B) and across different depths of the recording (Suppl. 2C). To investigate the origin of frequency patches, we tested whether individual patches correspond to the beating of individual cells.

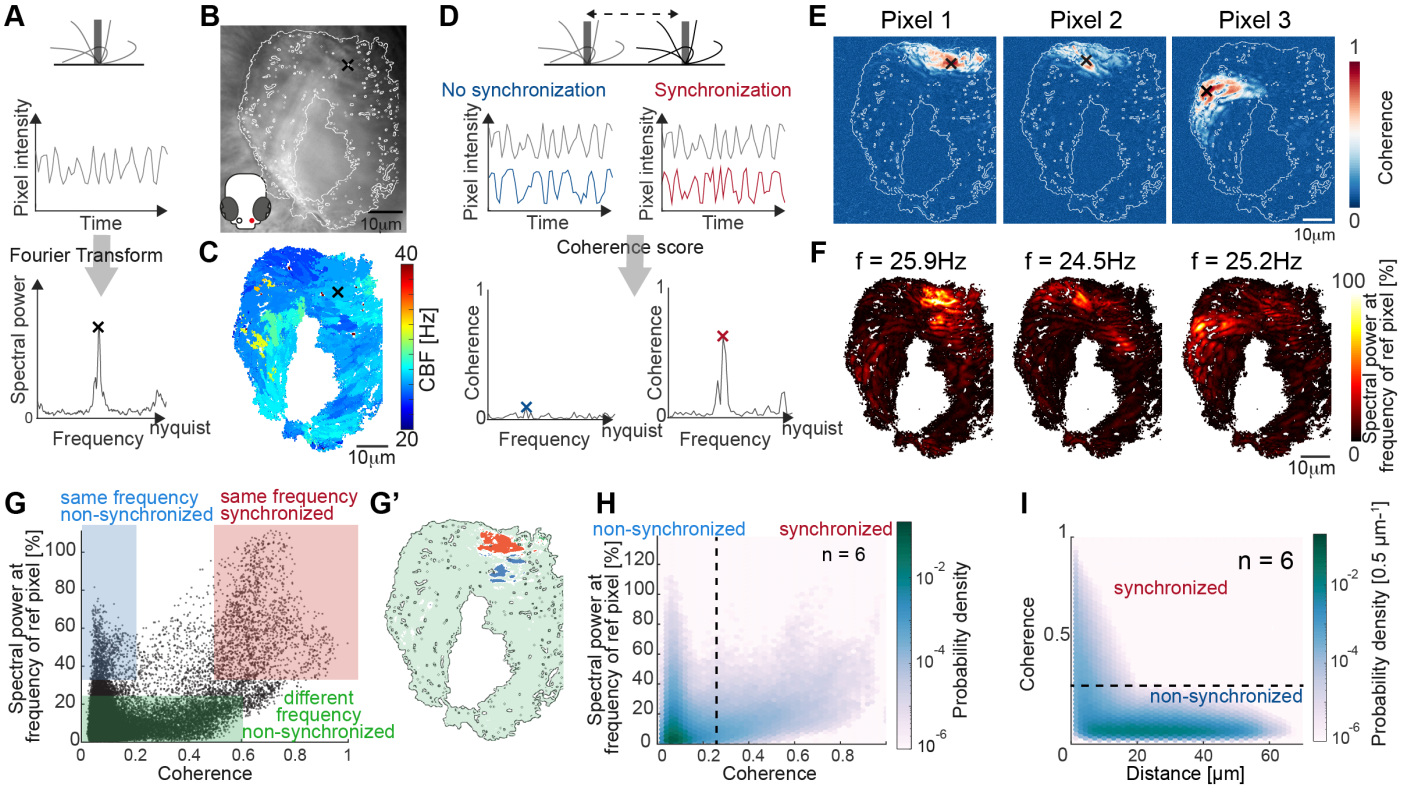

FIGURE 2: Spectral analysis of ciliary beating reveals local coherence but global heterogeneity*(A) Schematic spectral analysis of a reference pixel. As cilia move through a pixel (black rectangle), the pixel intensity fluctuates. The Fourier transform of pixel intensity time series (top), with peak frequency indicated (bottom). (B) Raw image frame of a representative light transmission recording in the left nose of a 4-day old zebrafish larva overlaid with the region representing ciliary beating (white line). (C) Frequency map of nose pit depicting peak frequency for each pixel. (D) Schematic depicting how the peak coherence measures ciliary synchronization. Note that unsynchronized pixels (blue) have low coherence throughout the frequency spectrum (left), while synchronized pixels (red) have a high coherence at the ciliary beating frequency (right). (E) Peak coherence for three reference pixels (indicated with black crosses) with all other pixels in a recording. (F) Spectral power evaluated at the frequency of the reference pixels (f = 25.9 Hz; 24.5Hz; 25.2 Hz) (G) Relationship between coherence and spectral power is plotted for a representative example (Pixel 1 of panel E). Three regions of interest are identified: synchronized pixels with high coherence and high spectral power at the frequency of Pixel 1(red, coherence ≥ 0.5 and spectral power ≥ 33.3%), non-synchronized pixels with high spectral power at the frequency of Pixel 1 but low coherence (blue, coherence ≤ 0.2 and spectral power ≥ 33.3%), and non-synchronized pixels with low spectral power at the frequency of Pixel 1 and low coherence (green, coherence ≤ 0.6 and spectral power ≤ 22.2%). Note that very few pixels show low spectral power but high coherence. (G') Note that synchronized (red) and non-synchronized (blue) pixels in (G) are not spatially overlapping in the nose. (H) An average of 6 reference pixels across 6 fish represented as a probability density.) (I) The relationship between coherence and pixel distance is plotted for an average of 6 fish as a probability density. Note that pixels located within 20 µm tend to be more coherent.*

Specifically, we examined cilia beating in transgenic animals expressing GFP sparsely in multiciliated cells of the nose (*Et(hspGGFF19B:Gal4)Tg(UAS:gfp)*[43]). We then recorded cilia beating sequentially with light-sheet microscopy, where we can identify individual cells, and light-transmission microscopy, where we can record the entire cilia carpet, and compared their CBF maps. We observed that the CBF of an individual cell corresponds better to that of the frequency patch than to the rest of the cilia carpet (Suppl. 2D), suggesting that cilia on the same cell beat at a similar frequency. Taken together, the presence of local frequency patches rules out a global synchronization in our system but still complies with a local synchronization across neighboring cells.

We asked next if cilia indeed synchronize, i.e., display not only the same CBF, but keep a fixed phase relation. To analyze cilia synchronization in the zebrafish nose, we adopted a measure inspired from neuroscience, the magnitude-squared coherence [52, 53, 54]. This measure, which has also been referred to as cross-correlation in Fourier space, reports the correlation of two signals across frequencies, independent of a phase lag between them. In theory, we should observe high coherence at the CBF only for synchronized cilia with fixed phase relationship, and not for unsynchronized cilia beating at the same frequency accidentally without fixed phase relation (Fig. 2D).

To measure the degree of coherence between pixels and hence cilia, we calculated the coherence score for one reference pixel with all other pixels in the recording, revealing so-called coherence domains surrounding the reference pixel (Fig. 2E). To relate coherence to CBF, we recovered the spectral power for the peak frequency of the reference pixel across the entire map (Fig. 2F) and compared the coherence score to the spectral power for all pixels of the recording (Fig. 2G). We observed that the peak frequency of the reference pixel is dominant in the entire coherence domain (note the similarity in coherence and frequency domains in Fig. 2E-F also shown in the red area in Fig. 2G-G'), confirming that cilia beat at (approximately) the same frequency when synchronized. Occasionally, the frequency domain extended to a region not in the coherence domain (blue highlight in Fig. 2G-G'), suggesting that cilia can beat at the same frequency by coincidence. As expected, if two pixels or cilia are not oscillating at the same frequency, they are not synchronized (green highlight, Fig. 2G).

Since the coherence appeared to be organized in domains (Fig. 2E-G'), we next calculated the coherence for all signal pixels in the recording and related it to the Euclidian distance separating the two pixels. We saw that, similarly to the reference pixel analysis (Fig. 2E), the coherence score quickly drops at approximately 20 µm (Fig 2I). In comparison, the diameter of a cell is 4.17-4.71 µm. Altogether, we propose the coherence score and the coherence versus distance as methods to quantify synchronization within a cilia carpet. Application of these methods to the nose pit indicates that cilia synchronize locally rather than globally.

Increasing viscosity reduces ciliary beating frequency and extends ciliary coherence

Since cilia synchronization appears to be local in nature, we asked whether changes in cilia beat dynamics can influence the spatial extent of their synchronization. To test this, we exposed the zebrafish nose to surrounding mediums of increasing viscosity. We chose to apply methylcellulose based on its reversible and non-invasive properties, and prior work suggesting that viscosity change can affect synchronization between cilia [16, 55]. By increasing methylcellulose concentration in a stepwise manner, we found that the CBF decreases upon increases in viscosity of the surrounding medium (Fig 3A-B & Suppl. 3C), similarly to previous reports [16, 56, 57].

Next, to probe the impact of viscosity on synchronization, we calculated the coherence versus distance for all pixels in the recordings (Fig. 3C). To visualize changes in the distribution, we plotted the difference from the baseline for the different conditions (Suppl. 3A) and observed that the number of coherent pixel pairs increased in the 5-20 µm distance range when viscosity increased. To quantify this effect, we compared the mean coherence (Fig 3D) and the fraction of coherent pixels using a threshold of coherence > 0.25 (Suppl. 3B) across distance bins (width = 0.5µm). We observed a significant effect of high viscosity conditions for both measures (Suppl. 3C), suggesting that increasing viscosity improves the synchronization strength between pixels with distance in the 5-20 µm range

Increasing the viscosity of the surrounding medium and thus the hydrodynamic load acting on beating cilia was previously shown to change the waveform of cilia beating [21, 56, 57], a phenomenon termed waveform compliance [58]. While this could in principle explain the improved synchronization observed in the zebrafish nose (Fig 3D, Suppl. 3B), changes in cilia waveform, if present, were too small to detect. Specifically, we performed light-sheet microscopy on multiciliated cells sparsely expressing GFP in their cilia upon increasing viscosity conditions. The cells were imaged from a transverse angle to allow manual reconstruction of the cilia beating waveform. By applying our FFT-based analysis on the light-sheet recordings, we observed a decrease in CBF, matching the light transmission experiment (Suppl. 3C&D). Similarly, kymographs revealed changes in the frequency and kinetics of ciliary beating (Suppl. 3E-E'). Manual tracking of cilia waveforms did not reveal obvious alterations in the ciliary beat

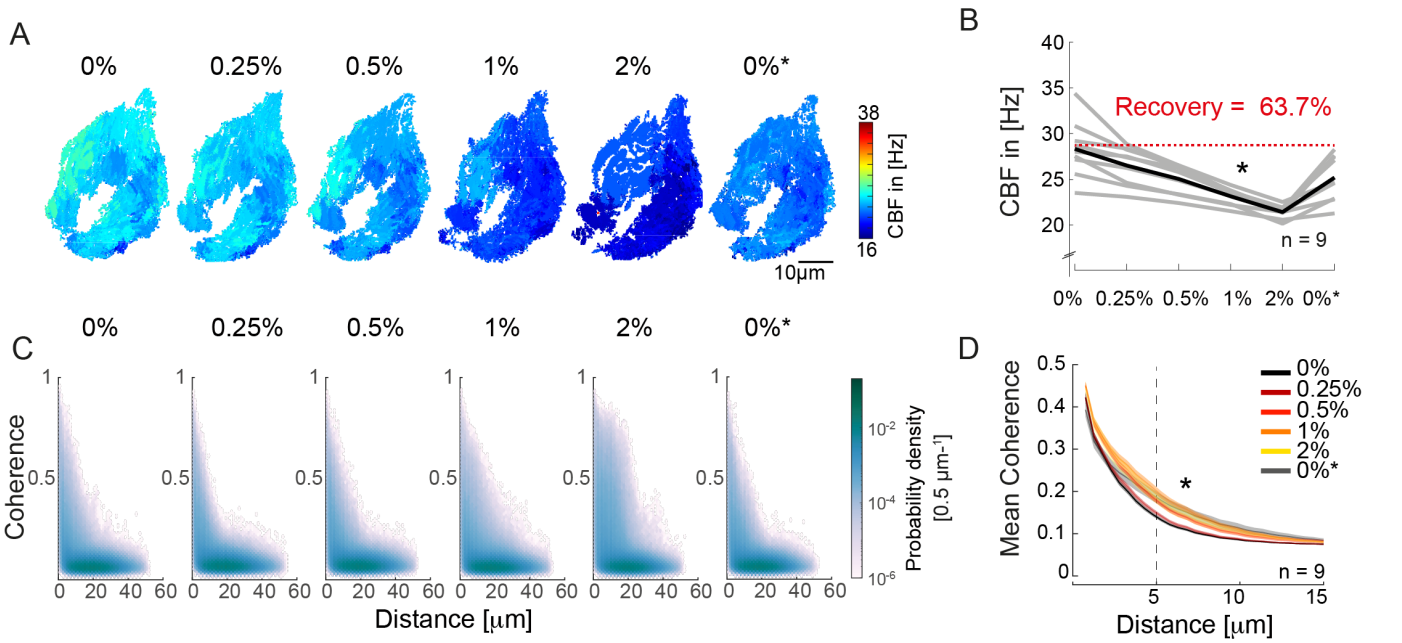

FIGURE 3: An increase in fluid viscosity decreases ciliary beat frequency and extends the spatial range of cilia coherence *(A-B) Ciliary beating frequency decreases under increasing viscosity conditions (0-2% methylcellulose) and partially recovers upon re-exposure to 0% methylcellulose (0%*). (A) Representative example of ciliary beat frequency (CBF) maps of a 4-day old zebrafish nose. (B) CBF for n = 9 (grey) and average in black. A repeated measures ANOVA (*) indicates a significant effect of viscosity conditions on CBF (p = 0.003; n = 9). (C-D) Ciliary coherence extends with increased fluid viscosity. (C) A representative example of pairwise coherence versus distance for different viscosity conditions (Coherence bin width = 0.04/bin; Distance bin width = 0.5µm/bin). (D) Mean coherence across distance bins (width = 0.5µm) for different viscosity conditions shows that coherence domains expand for conditions of increased viscosity. Mean curves and standard error of the mean are plotted (n = 9). ANOVA-N indicates a significant effect of viscosity conditions on mean coherence across distances ($p = 3 \cdot 10^{-5}$). CBF = Ciliary Beat Frequency.*

amplitude, even though our approach may not be sensitive enough to observe slight variations in waveform (Suppl. 3F). We argue that the combined use of coherence and frequency analyses is more comprehensive for investigating changes in the dynamics of cilia beating than the use of kymographs and manual tracing. Using this combined approach, our results indicate that an increase in viscosity both changes cilia beating properties and improves short-range synchronization.

Persistent tissue-scale patterns of metachronal coordination differ for left and right nose

Collections of motile cilia can coordinate their beat into traveling waves of cilia phase, so-called metachronal waves [59, 60, 61, 62, 63]. Given the heterogeneous beating frequency and lack of global synchronization, we asked whether metachronal waves emerge in our system.

Metachronal waves have been commonly detected using kymographs [60, 61]. Using such an approach on our light transmission recordings (Fig. 4A-A'), we observed that metachronal-like activity is present in the zebrafish nose, but is not stable over time, as shown by analyzing the same recording during two different time windows (Fig. 4A'). This suggests that these waves are highly dynamic in space and time and studying them by means of kymographs is not only time-intensive and difficult to quantify but also prone to misinterpretations. In agreement with our findings, simulated metachronal waves may display defects [18], but maintain a stable direction over time [18, 27]. Hence, we developed an automated detection method to better visualize the properties of metachronal waves, including direction and wavelength, based on the phase angle of our FFT-based CBF detection method (Fig. 4B).

To obtain robust phase angles across the ciliated epithelium, we first segmented the frequency map into distinct patches, so that neighboring pixels with similar frequency (CBF bin = 0.54 Hz) were assigned to the same patch. We then extracted the phase angle from the Fourier spectrum for the dominant frequency of that given patch. We decided to extract phases from segmented patches because i) phases extracted for different frequencies are not comparable and lead to noisy signals precluding further analysis, and ii) for timeseries of finite length, phases of Fourier modes at nearby frequencies are correlated. This analysis led to the identification of phase angles for each pixel of the recording (Fig. 4B right and Suppl Video S1&2). Next, to translate phase information to wave direction and wavelength quantifications, we extracted image gradient vectors from each patch separately (Fig. 4C). This allowed us to quantify and plot both wave direction and wavelength, by calculating the mean vector direction and the mean vector length,

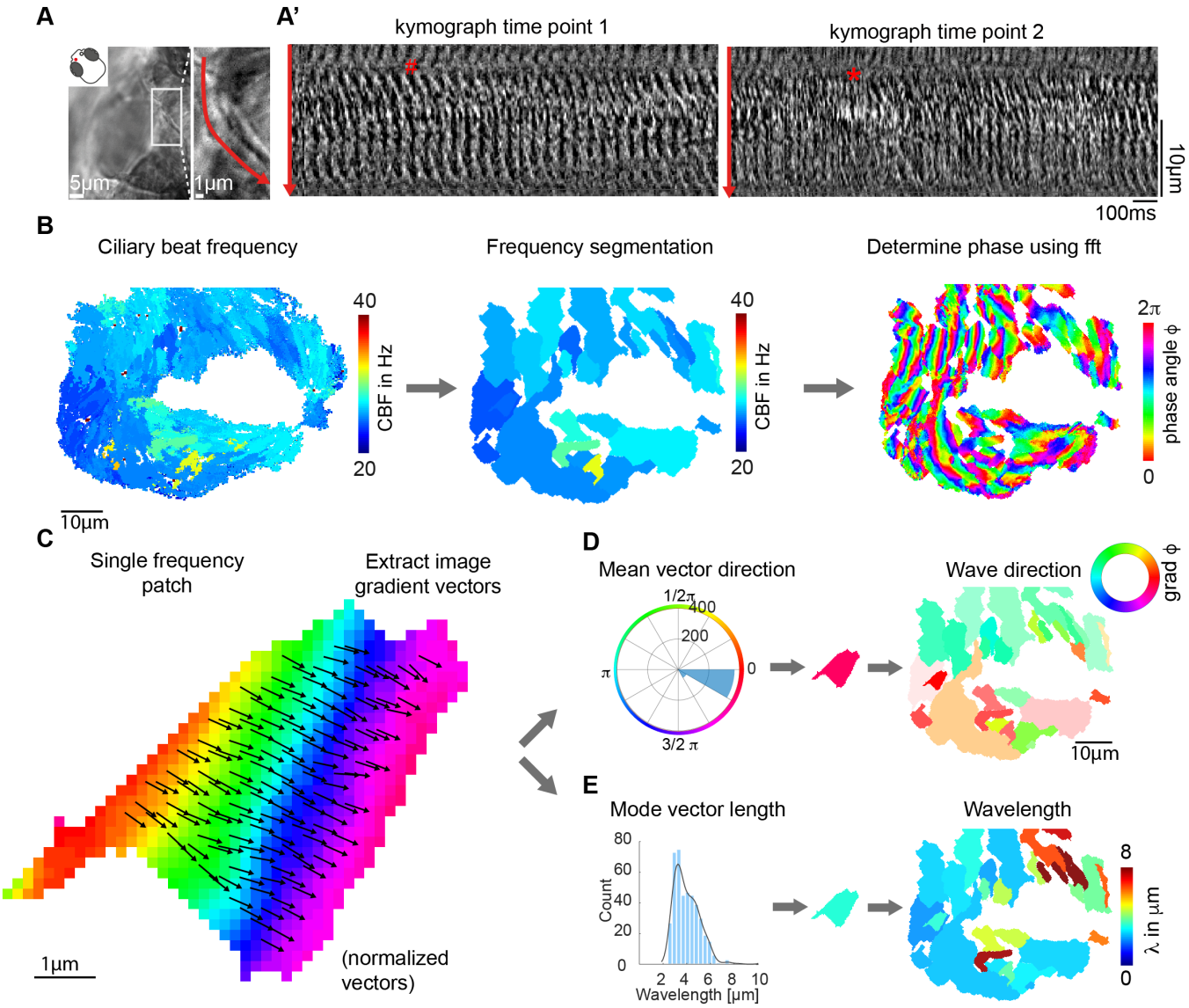

FIGURE 4: Ciliary beating displays local metachronal coordination

(A-A') Metachronal coordination observed using a conventional kymograph-based analysis. (A) A kymograph was drawn (red line in inset, representing transverse ciliary beating) on a light transmission recording of a zebrafish nose at 4dpf. (A') Kymographs of ciliary beating in the same location at different time-points. Note the orderly pattern in the left panel (#) versus the disorderly pattern in the right panel (*). (B-D) Pipeline to measure metachronal coordination based on a phase angle method. (B) Neighboring pixels with similar frequency (beat frequency map, left) are segmented into patches (center). Phase angles are determined from Fourier transforms evaluated at the prominent frequency of each segmented patch (right). (C) Analysis proceeds for each patch by extracting an image gradient, as shown by the arrows. (D-E) The mean direction of the gradient vector characterizes wave direction – with transparency representing the inverse circular standard deviation (D, right) while its length determines the wavelength (E, left). Scale bars, 10µm. See also video S1-S3.

respectively (Fig. 4D). Using this approach, we found that the wave directions form regular patterns (Fig. 4D), which are stable over time (Suppl. 4A & suppl. Video S3), across depth (Suppl. 4B), and not affected by increasing viscosity (Suppl. 4C). In contrast, we observed a large variability of wavelength in space and time (Suppl. 4A-C). In summary, our results indicate that metachronal waves are present in the zebrafish nose and that their wave direction remains stable.

We next asked whether the observed pattern of metachronal wave direction is a consistent feature across different individuals. To compare multiple noses, we first aligned multiple recordings of left noses and found that the pattern of wave directions is highly comparable across noses, while wavelengths vary (Fig. 5A & Suppl. 5A). Next, to compare left noses with right noses, we mirrored and aligned right noses so that they had the same mediolateral orientation as the left noses. Surprisingly, we observed that the wave directions between left and right noses are consistently different (Fig. 5B & Suppl. 5A). To relate the direction of the metachronal waves to cilia beating, we measured the cilia beat direction. The

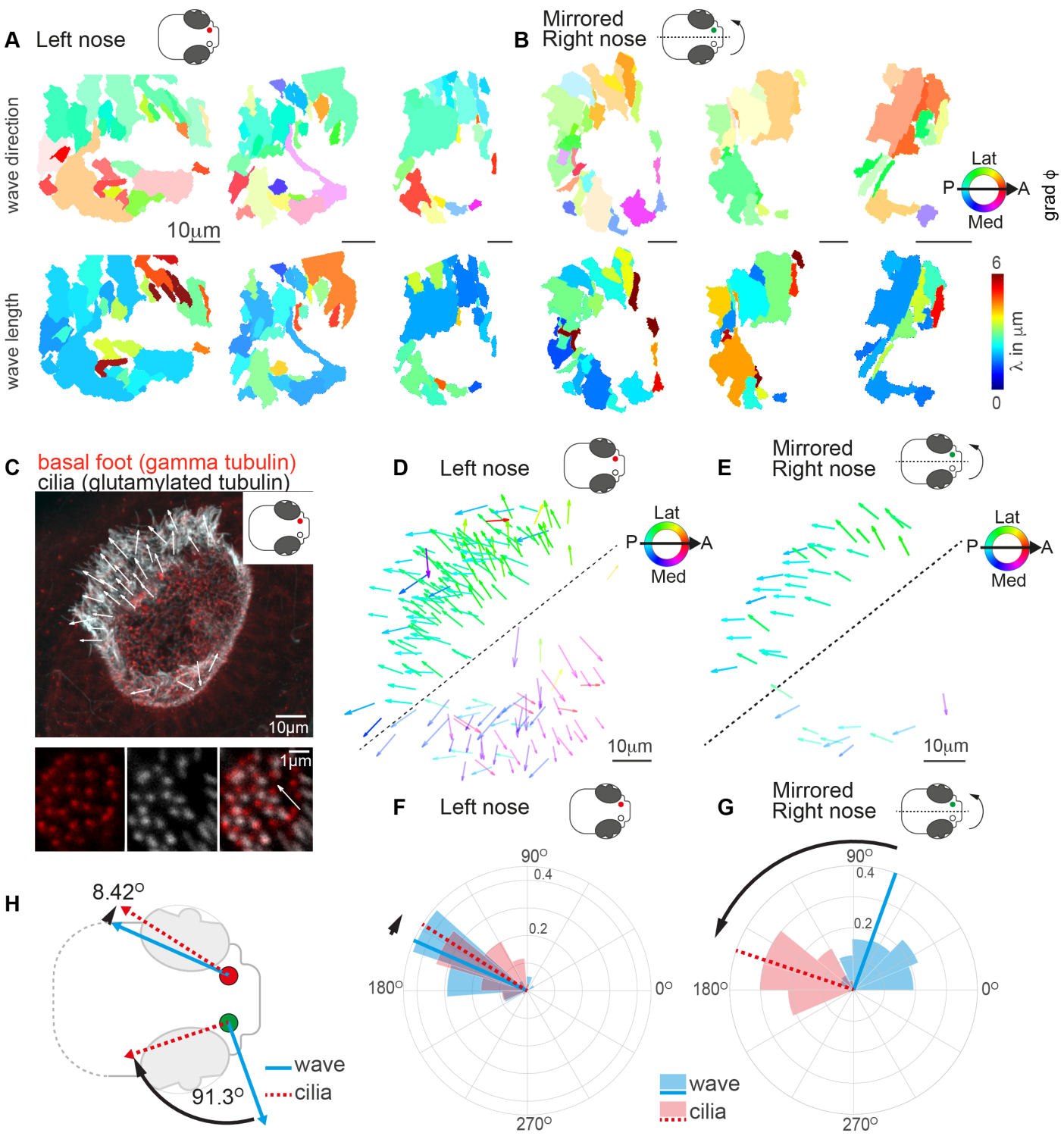

FIGURE 5: Metachronal wave directions are chiral

(A-B) Wave direction (top) and wavelength (bottom) for three left (A, red) and three mirrored right (B, green) noses show asymmetry in the wave direction between the left and right noses. Transparency reflects the inverse circular standard deviation. (C) Immunohistochemistry on a left nose stained for gamma-tubulin (basal body marker, red) and glutamylated tubulin (cilia marker, white). Zoom-in on a cell obtained at higher magnification displays how gamma-tubulin and glutamylated-tubulin stains are offset, allowing to determine ciliary beat direction. (D-E) Overlay of all ciliary beat directions in the left (D; n = 10) and mirrored right (E; n = 3) noses. Individual arrows refer to the cilia orientation of individual cells across fish. Direction is color-coded. Note a clear distinction between the latero-posterior and medial part of the nose indicated by a dashed line. (F-G) Quantification of all ciliary beat directions as compared to metachronal wave directions for left (F) and mirrored right (G) noses. Plotted are the mean directions per fish for the latero-posterior part of the noses (above dashed line in D and E). (H) Schematic of the wave directions in the left versus the right nose. Note that the offset between the mean ciliary beat directions (red) and metachronal waves directions (blue) is 8.42° for the left nose (same direction; symplectic) and 91.3° (to the right; dexioplectic) for the right nose. Scale bars are 10µm.

cilia beat direction is set developmentally [37, 40, 42, 64, 65] and can be inferred from the location of the cilia basal foot, which points towards the cilia beat direction [10, 66]. To discern the cilia beat direction for each cell, we stained the 4dpf zebrafish nose for basal feet (gamma-tubulin) as well as the cilium (glutamylated tubulin) (Fig. 5C & Suppl. 5B). We found that the ciliary beat direction is consistent across fish (Fig. 5D) and is mirrored for the left and right noses (Fig. 5D& F). In contrast, we observed a stark difference in the angle between cilia beating and the wave direction between left and the right noses, with an angle of 8.42º for left noses (Fig. 5F) and 91.3º for right noses (Fig. 5G). Ciliary beating of multiciliated cells have been shown to have a certain rotational component, which introduces a defined chirality of the cilia beat [16]. Moreover, in modeling studies, this chirality was shown to set a direction of emergent metachronal waves different from the cilia beat direction [18, 27]. The broken mirror-symmetry due to chiral cilia beat patterns explains why the direction of metachronal waves can be rotated relative to the main cilia beat direction. However, it cannot explain why we observe different angles for the left and right nose.

In conclusion, by designing novel ways to quantify cilia synchronization and the spatial organization of cilia within a tissue in dense carpets, we revealed the presence of metachronal waves with stable wave directions that are different for the left and right nose.

Metachronal coordination enhances fluid pumping and reduces steric interactions but does not affect fluid flow direction

To investigate the role of metachronal coordination in cilia carpets on their physiological function of fluid pumping, we resorted to a computational model. Specifically, we used a recently established multi-scale model of a regular array of cilia [27, 36], which uses detailed hydrodynamic computations and an experimentally measured beat pattern from *Paramecium* [16]. Importantly, this model allows us to disentangle the roles of hydrodynamic and steric interactions.

The computational model enables us to probe traveling waves with different directions and wavelengths in a cilia carpet as shown in Fig. 6A, where each dot in the hexagonal plot represents a different traveling wave solution with different wave length λ and direction angle θ represented by a wave vector $(k_x,k_y) = 2\pi/\lambda\,(-\sin\theta, \cos\theta)$. Using this model, we first investigated how different traveling waves impact the pumping rate per cilium and the mean direction of fluid flow. We observed that the pumping rate is close to its minimum when all cilia beat with the same phase, i.e., for in-phase cilia beating with $(k_x,k_y)=(0,0)$ (Fig. 6B). In contrast, if cilia beat in the form of a metachronal traveling wave with finite wavelength λ, the pumping rate increases significantly. We observed a stronger increase in pumping rate for symplectic or antiplectic metachronal coordination (for which the wave vector is parallel to the direction of the cilia effective stroke, $\theta = 0^0, 180^0$), as compared to dexioplectic or laeoplectic metachronism (for which the wave vector is perpendicular to the direction of the effective stroke, $\theta = \pm 90^0$). The observed change in pumping rate is a result of hydrodynamic interactions between cilia: if cilia move in opposite directions for an antiplectic wave, destructive interference of flow fields implies that the hydrodynamic load increases for each cilium; as a consequence, more fluid is pumped per cilium and beat cycle. Also, hydrodynamic interactions are stronger in the direction of an applied force as compared to the direction perpendicular to the force, accounting for the difference observed between sym-/anti-plectic and lae-/dexio-plectic. Although this increase in hydrodynamic load also slows down the collective frequency of cilia beating [27], this second effect is not strong enough to revert the increase of pumping rate due to enhanced hydrodynamic load. For numerical reasons, our computational model allows only a dilute cilia density of 0.0036 μm^{-2} for which cilia do not collide. For higher cilia densities, we expect the change in pumping rate to be even more pronounced [18, 24].

Next, we investigated the impact of different metachronal wave solutions on the direction of cilia-generated fluid flow. As shown in Fig. 6C, we observed that the flow direction is virtually independent of the direction and wavelength of metachronal waves with a variability of less than $\pm 5^0$ for the chosen cilia density. Hence, our results revealed that metachronal waves are beneficial for fluid pumping but do not impact majorly the direction of fluid flow.

We then probed how local synchronization impacts fluid pumping. We previously showed that above a characteristic phase noise level, global synchronization is lost but local synchronized domains persist (27). Since long-range hydrodynamic interactions decay near a wall as inverse cubed distance ($\sim d^{-3}$), hydrodynamic interactions between distant cilia should have little impact on the rate of fluid pumping, and in fact were previously shown to be dispensable for our computational model [27]. Hence, we expect that in a cilia carpet exhibiting metachronal coordination, the main determinant affecting fluid pumping is phase noise between nearby cilia. Correspondingly, we investigated the impact of increasing phase noise on fluid pumping in four possible scenarios: *(i)* the dexioplectic wave with wave vector $\mathbf{k}_l$ that emerges spontaneously in the computational model [27], *(ii)* the dexioplectic wave observed in the right zebrafish nose (where $\theta \approx 90^o$, Figure 5H), *(iii)* the antiplectic wave that maximizes fluid pumping, and *(iv)* in-phase cilia beating. We observed that, for the perfect dexioplectic wave, the

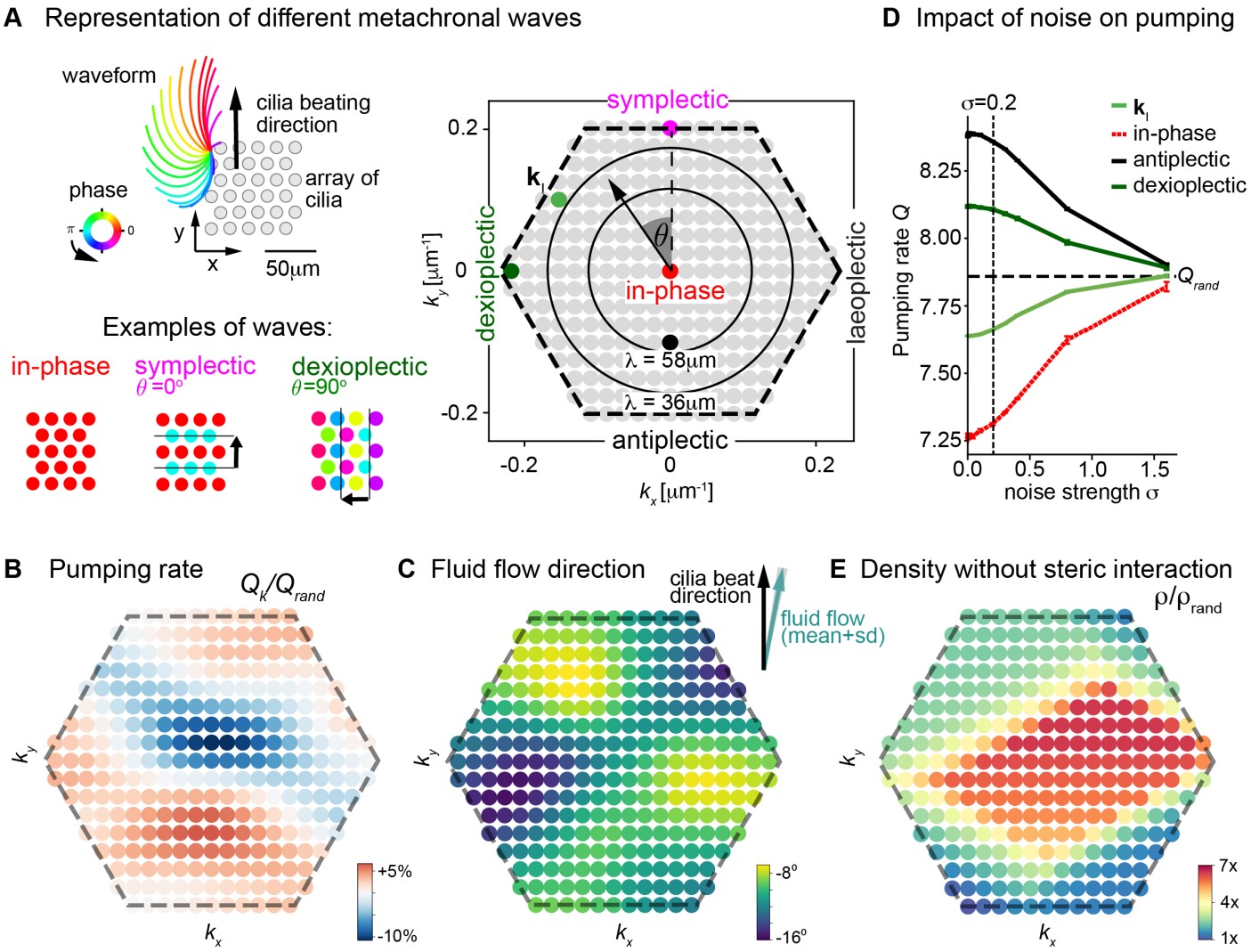

FIGURE 6. Metachronal coordination enhances fluid pumping and reduce steric interactions, but does not affect fluid flow direction.

(A) Possible traveling wave solutions in a computational model of a cilia carpet. Left: *Cilia are arranged on a triangular lattice (gray dots), with three-dimensional cilia beat pattern from* Paramecium *(not to scale, cilia length 10μm). Three example wave solutions are highlighted: in-phase beating, symplectic wave, dexioplectic wave. Wave fronts are indicated by black lines and the wavedirection by an arrow, while the color code of cilia base points represents cilia phase.* Right: *Visualization of the set of all possible wave solutions as function of wave vector* $\mathbf{k}=(k_x,k_y)$, *where the distance from the origin encodes the wavelength of the wave as* $\lambda = 2\pi/|\mathbf{k}|$ *and the directional angle* θ *encodes the direction of the wave relative to the direction of the effective stroke of the cilia beat. Example waves from left panel are highlighted as colored dots. (B) Pumping rate Q per cilium computed for different wave solutions, with each wave represented by a color-coded dot as in hexagon plot of panel A (normalized by pumping rate* $Q_{rand} \approx 7.87$ μm³/ms *for cilia beating with random phase relationship). (C) Direction of cilia-generated flow (averaged over one beat cycle) for different wave solutions relative to the direction of the effective stroke of the cilia beat; note that the range of the color bar spans only 10°. Mean±standard deviation is shown in inset. (D) Pumping rate per cilium for four selected wave solutions (as indicated in hexagon plot of panel (A) as function of a noise strength* σ *(see text for details). Dashed line indicates mean pumping rate for cilia beating with random phase relationship (*Q_{rand}*). (E) Critical density* ρ *of a cilia carpet below which steric interactions between cilia arise for different wave solutions; density* ρ *is normalized relative to a critical density for cilia beating with random phase relationship,* $\rho_{rand} = 0.015$ μm^{-2}.

rate of fluid pumping approximately equals that for cilia beating with a random phase relationship, while the pumping rate is substantially higher for the most efficient antiplectic wave and a dexioplectic wave with $\theta = 90°$ (Fig. 6D). Generally, if random perturbations of cilia phase remain small (standard deviation $\sigma<0.2$), the pumping rate is only moderately changed. For stronger phase noise ($\sigma>1$), the pumping rate attains a constant value, irrespective of the underlying wave solution, as cilia essentially beat with random phase relationship. Taken together, our results show that cilia carpets exhibiting metachronal coordination can tolerate some level of noise of cilia beating for their physiological function of fluid pumping.

Besides improving fluid flow, metachronal waves may also prevent steric interactions between cilia, which would slow down their dynamics. To probe the relevance of steric interactions, we computed for each wave solution a critical density $\rho(\mathbf{k})$ at which cilia do not collide (Fig. 6E). We observed that this critical

density is substantially higher than a corresponding density ρ_{rand} defined for cilia beating with random phase relationship. In fact, this critical density is minimal for in-phase cilia beating. However, for in-phase beating, the predicted pumping rate is also minimal. In contrast, symplectic and dexioplectic metachronal coordination allow for both an elevated pumping rate and denser cilia packing. We speculate that metachronal coordination may represent an evolutionary solution to the trade-off choice of both realizing a high pumping rate per cilium (which favors metachronal coordination with short wavelength, see Fig. 6B) and a high cilia density (which favors in-phase synchronization, see Fig. 6D), which together set the pumping efficiency of a cilia carpet. This refines a previous hypothesis by Machemer, who proposed that dexioplectic waves reduce steric interactions as compared to symplectic or antiplectic waves [16].

In conclusion, our results revealed that local synchronization is a prerequisite for efficient cilia beating in dense cilia carpets. We propose that local order allows realizing almost the maximal possible rate of fluid pumping and reduces steric interactions.

DISCUSSION

By using novel tools to quantify ciliary synchronization *in vivo* and a computational model, we put forward the notion of local but not global synchronization as the expected form of cilia coordination in the presence of noise and perturbations. Even with only local synchronization of cilia, a tissue-scale metachronal coordination with distinct pattern of wave directions is possible in cilia carpets. Indeed, we observed in a zebrafish model system tissue-scale patterns of metachronal waves, which were consistent across individual animals, but different for left and right noses. This difference in wave directions is not a mere consequence of different patterns of cilia alignment, but instead points at an important role of the chirality of the cilia beat. On the basis of computational results, we propose that local synchronization is sufficient to pump fluids at an almost maximal rate.

In this study, we chose to study multiciliated cells in the developing zebrafish nose. We identified that although these cells bear a reduced number of cilia as compared to mammalian tissues or *Xenopus* embryonic skin, they retain a ciliary density similar to these other multiciliated epithelia due to their smaller apical area [58]. In principle, the apical size of cells should not matter for the physics of cilia synchronization. As a small caveat, it is possible that a ciliated epithelium made of smaller cells may be more heterogeneous due to higher divergence in cilia properties across cells. Yet, since the density of cilia is a key property for synchronization of motile cilia [20, 38], we argue that the zebrafish nose is an appropriate model for studying coupling mechanisms within and across cell boundaries in a naturally dense cilia carpet, which is highly accessible for imaging experiments.

Using Fourier-based analyses, we observed that motile cilia in the zebrafish nose beat at different frequencies, both within the organ and across fish. It appears that those frequencies are linked to separate cells and raises the question as to why different cells have distinct frequencies. The beating frequency may depend on the number of cilia on the cell [38], the age of the cell or animal [1], but likely not the length of the cilium [67, 68]. Beat frequency may also relate to the level of synchronization across cilia. In fact, it was shown that upon synchronization the emergent frequencies of two oscillators converge to the same value as long as the intrinsic frequencies are similar enough [20, 29, 38, 69]. Moreover, cilia should beat faster (or slower) when they are synchronized in-phase (or in anti-phase) because the hydrodynamic friction acting on an individual cilium decreases (or increases) [18, 26, 27 , 38]. Of note, the cilia beat frequencies reported here do not represent the intrinsic beat frequencies of individual cilia, but instead the emergent frequency when a cilium is interacting with its neighbors. Nevertheless, in our system, we observed that beat frequencies are widely distributed, suggesting that there is no synchronization on a global, tissue scale. This also agrees with experimental data in airway human cells [70] and modeling work showing that frequency dispersity and active noise in cilia beating limit synchronization to the local scale [23, 36]. To probe how global versus local synchronization affects the transport of fluid, we turned to a computational approach. We highlight how local synchronization is a prerequisite to reduce steric hindrance in dense cilia carpets. Moreover, the pumping rate of a cilia carpet is robust against moderate levels of phase noise between neighboring cilia, while it should be independent of hydrodynamic interactions with distant cilia, suggesting that locally synchronized cilia can achieve fluid pumping at an almost maximal possible rate. Our results thus complement a previous study suggesting a beneficial effect of slight disorder in the cilia polarity for effective fluid transport in the lung [10], by highlighting beneficial effects of local order.

Previous methods to investigate coordinated ciliary movement include spatial correlation approaches [61, 71], measures of phase similarity [39], or spatial correlation functions [60, 70]. However, these approaches are either not automated, or complicated to interpret. In this study, we applied another measure for synchronization known from neuroscience, the magnitude-squared coherence [52, 53]. This measure proved to be very robust to detect synchronization across pixels. Synchronized oscillators should beat at the same frequency. Indeed, we observed that our coherence score only reported pixel pairs oscillating at the same frequency. However, having the same frequency is only a necessary and not a sufficient condition.

Indeed, we noticed that not all pixel pairs oscillating at the same frequency were coherent, in particularly when pixels were far apart and only "accidentally" shared the same frequency. Using this measure, we observe that coherence rapidly decays at a pixel distance of approximately 20 µm, which is larger than the diameter of a cell (4.17-4.71 µm), and longer than the length of a single cilium of approximately 9 µm. We thus have an indirect, but not yet direct proof that coherence domains cross cell boundaries. It remains to be understood what sets the size of the observed coherence domains. Generally, a stronger coupling between cilia promotes larger domains, while active noise of the cilia beat, dispersity of intrinsic cilia beat frequency, and imperfect cilia alignment should cause smaller domains [27, 36].

Our results revealed that coherence domains slightly increase in size when the viscosity of the surrounding medium is increased. This complements previous findings by Machemer that changing viscosity can change the direction of metachronal waves in cilia carpets in unicellular *Paramecium* [16]. We suppose that changing the viscosity of the surrounding medium slightly changes the cilia beat pattern and therefore the synchronization coupling between nearby cilia. Indeed, previous literature showed that shape and speed of the cilia beat changes upon increased viscosities or hydrodynamic load [21, 56].

Traveling waves of ciliary phase, in the form of so-called metachronal waves, have been previously observed in ciliated system, particularly in ciliates [60, 61]. They are often highlighted as a feature of synchronized cilia [9, 62], which promote efficient fluid transport [18]. Using a novel analysis method based on the phase of the Fourier transform of time-lapse recordings, we revealed coherent patterns of metachronal wave directions in nose pits, which were consistent across individual fish. Intriguingly, wave patterns were different for the left and right nose, with a symplectic wave in the latero-posterior region of the left nose (waves propagating in the direction of cilia orientation, [17]), but a dexioplectic wave in the right nose (wave direction rotated counter-clockwise by a 90° angle relative to cilia orientation when viewed from the distal side). We speculate that chiral cilia beat patterns may be different for the left and right nose, respectively, since different cilia beat patterns will give rise to different dominant metachronal waves [26], as observed for different metazoan species [17]. Usually, only one type of metachronism is observed in a single species, and even in a single systematic group. The zebrafish model system established here thus opens the unique opportunity to study two different fundamental types of metachronal coordination, symplectic and dexioplectic, in a single species.

Using hydrodynamic computations, we showed that metachronal coordination hardly changes the direction of cilia-generated fluid flow. Hence, it is unlikely that the different metachronal wave patterns observed between the left and right zebrafish nose and in different species in general affect the direction of fluid flow and thus their physiological function. However, metachronal coordination enhances the rate of fluid pumping and at the same time reduces steric interactions at higher cilia density. We speculate that observed metachronal waves may provide an optimal trade-off between a high pumping rate per cilium and a high cilia density within a cilia carpet.

In conclusion, we describe here an accessible *in vivo* model system and novel analytical methods to quantify the properties of the cilia beat as well as emergent synchronization in ciliated epithelium in an unbiased manner. Using these tools, we show that local synchronization is sufficient for coherent patterns of metachronal coordination, which expectedly allows to realize almost the maximal rate of fluid pumping.

ACKNOWLEDGEMENTS

We thank V Nguyen, A Nygaard and the Trondheim fish facility team for their technical support, E Yaksi and F Palumbo for the helpful discussions. This work was supported by a Boehringer Ingelheim Fonds fellowship (C.R), RCN FRIPRO grants 314189 (N.J.Y.). B.M.F. is supported by a DFG-Heisenberg grant (FR3429/4-1), as well as 'Physics of Life' (Cluster of Excellence EXC-2068) and *cfaed*. A.S. is supported by the DFG priority program SPP1726 'Microswimmers' (FR3429/1-1 and FR3429/1-2 to B.M.F.).

AUTHOR CONTRIBUTIONS

Conceptualization, N.J.-Y., B.M.F., and C.R.; Methodology, S.B., C.R., J.N.H, M.E. and A.S.; Formal Analysis, C.R., S.B., A.S., J.N.H., B.M.F., and N.J.-Y.; Writing, N.J.-Y., B.M.F., and C.R.; Review & Editing, all authors; Funding Acquisition, N.J.-Y., B.M.F., and C.R.; Supervision, B.M.F. and N.J.-Y.

DECLARATION OF INTEREST

The authors report no conflict of interest.

REFERENCES

1. Olstad EW*, et al.* Ciliary Beating Compartmentalizes Cerebrospinal Fluid Flow in the Brain and Regulates Ventricular Development. *Curr Biol* **29**, 229-241.e226 (2019).
2. Sawamoto K*, et al.* New neurons follow the flow of cerebrospinal fluid in the adult brain. *Science* **311**, 629-632 (2006).
3. Ringers C, Olstad EW, Jurisch-Yaksi N. The role of motile cilia in the development and physiology of the nervous system.

Philosophical Transactions of the Royal Society B: Biological Sciences **375**, 20190156 (2020).
4. Faubel R, Westendorf C, Bodenschatz E, Eichele G. Cilia-based flow network in the brain ventricles. *Science* **353**, 176-178 (2016).
5. Worthington Jr WC, Cathcart III RS. Ciliary currents on ependymal surfaces. *Annals of the New York Academy of Sciences* **130**, 944-950 (1966).
6. Date P*, et al.* Visualizing flow in an intact CSF network using optical coherence tomography: implications for human congenital hydrocephalus. *Scientific Reports* **9**, 6196 (2019).
7. Sternberg JR*, et al.* Pkd2l1 is required for mechanoception in cerebrospinal fluid-contacting neurons and maintenance of spine curvature. *Nature communications* **9**, 3804-3804 (2018).
8. Thouvenin O*, et al.* Origin and role of the cerebrospinal fluid bidirectional flow in the central canal. *Elife* **9**, (2020).
9. Bustamante-Marin XM, Ostrowski LE. Cilia and Mucociliary Clearance. *Cold Spring Harbor perspectives in biology* **9**, a028241 (2017).
10. Ramirez-San Juan GR, Mathijssen AJTM, He M, Jan L, Marshall W, Prakash M. Multi-scale spatial heterogeneity enhances particle clearance in airway ciliary arrays. *Nature Physics* **16**, 958-964 (2020).
11. Wallmeier J*, et al.* De Novo Mutations in FOXJ1 Result in a Motile Ciliopathy with Hydrocephalus and Randomization of Left/Right Body Asymmetry. *Am J Hum Genet* **105**, 1030-1039 (2019).
12. Ferreira RR*, et al.* Chiral Cilia Orientation in the Left-Right Organizer. *Cell Rep* **25**, 2008-2016.e2004 (2018).
13. Nonaka S*, et al.* Randomization of left–right asymmetry due to loss of nodal cilia generating leftward flow of extraembryonic fluid in mice lacking KIF3B motor protein. *Cell* **95**, 829-837 (1998).
14. Sanderson MJ, Sleigh MA. Ciliary activity of cultured rabbit tracheal epithelium: beat pattern and metachrony. *Journal of cell science* **47**, 331-347 (1981).
15. Brumley DR, Polin M, Pedley TJ, Goldstein RE. Hydrodynamic synchronization and metachronal waves on the surface of the colonial alga Volvox carteri. *Physical review letters* **109**, 268102 (2012).
16. Machemer H. Ciliary activity and the origin of metachrony in Paramecium: effects of increased viscosity. *Journal of Experimental Biology* **57**, 239-259 (1972).
17. Knight-Jones EW. Relations between Metachronism and the Direction of Ciliary Beat in Metazoa. *Quarterly Journal of Microscopical Science* **s3-95**, 503-521 (1954).
18. Elgeti J, Gompper G. Emergence of metachronal waves in cilia arrays. *Proc Natl Acad Sci U S A* **110**, 4470-4475 (2013).
19. Taylor GI. Analysis of the swimming of long and narrow animals. *Proceedings of the Royal Society of London Series A Mathematical and Physical Sciences* **214**, 158-183 (1952).
20. Brumley DR, Wan KY, Polin M, Goldstein RE. Flagellar synchronization through direct hydrodynamic interactions. *Elife* **3**, e02750 (2014).
21. Klindt GS, Ruloff C, Wagner C, Friedrich BM. Load Response of the Flagellar Beat. *Physical Review Letters* **117**, 258101 (2016).
22. Gueron S, Levit-Gurevich K. Energetic considerations of ciliary beating and the advantage of metachronal coordination. *Proceedings of the National Academy of Sciences* **96**, 12240-12245 (1999).
23. Guirao B, Joanny J-F. Spontaneous creation of macroscopic flow and metachronal waves in an array of cilia. *Biophysical journal* **92**, 1900-1917 (2007).
24. Osterman N, Vilfan A. Finding the ciliary beating pattern with optimal efficiency. *Proceedings of the National Academy of Sciences* **108**, 15727-15732 (2011).
25. Wollin C, Stark H. Metachronal waves in a chain of rowers with hydrodynamic interactions. *The European Physical Journal E* **34**, 1-10 (2011).
26. Meng F, Bennett RR, Uchida N, Golestanian R. Conditions for metachronal coordination in arrays of model cilia. *Proceedings of the National Academy of Sciences* **118**, e2102828118 (2021).
27. Solovev A, Friedrich BM. Synchronization in cilia carpets: multiple metachronal waves are stable, but one wave dominates. *New Journal of Physics* **24**, 013015 (2022).
28. Chakrabarti B, Fürthauer S, Shelley MJ. A multiscale biophysical model gives quantized metachronal waves in a lattice of beating cilia. *Proceedings of the National Academy of Sciences* **119**, e2113539119 (2022).
29. Quaranta G, Aubin-Tam M-E, Tam D. Hydrodynamics Versus Intracellular Coupling in the Synchronization of Eukaryotic Flagella. *Physical Review Letters* **115**, 238101 (2015).
30. Wan KY, Goldstein RE. Coordinated beating of algal flagella is mediated by

basal coupling. *Proceedings of the National Academy of Sciences* **113**, E2784-E2793 (2016).
31. Klindt GS, Ruloff C, Wagner C, Friedrich BM. In-phase and anti-phase flagellar synchronization by waveform compliance and basal coupling. *New Journal of Physics* **19**, 113052 (2017).
32. Soh AWJ*, et al.* Ciliary force-responsive striated fibers promote basal body connections and cortical interactions. *The Journal of cell biology* **219**, e201904091 (2020).
33. Polin M, Tuval I, Drescher K, Gollub JP, Goldstein RE. Chlamydomonas swims with two “gears” in a eukaryotic version of run-and-tumble locomotion. *Science* **325**, 487-490 (2009).
34. Ma R, Klindt GS, Riedel-Kruse IH, Jülicher F, Friedrich BM. Active phase and amplitude fluctuations of flagellar beating. *Physical review letters* **113**, 048101 (2014).
35. Goldstein RE, Polin M, Tuval I. Noise and synchronization in pairs of beating eukaryotic flagella. *Physical review letters* **103**, 168103 (2009).
36. Solovev A, Friedrich BM. Synchronization in cilia carpets and the Kuramoto model with local coupling: Breakup of global synchronization in the presence of noise. *Chaos: An Interdisciplinary Journal of Nonlinear Science* **32**, 013124 (2022).
37. Guirao B*, et al.* Coupling between hydrodynamic forces and planar cell polarity orients mammalian motile cilia. *Nat Cell Biol* **12**, 341-350 (2010).
38. Pellicciotta N*, et al.* Entrainment of mammalian motile cilia in the brain with hydrodynamic forces. *Proceedings of the National Academy of Sciences* **117**, 8315-8325 (2020).
39. Oltean A, Schaffer AJ, Bayly PV, Brody SL. Quantifying Ciliary Dynamics during Assembly Reveals Stepwise Waveform Maturation in Airway Cells. *American journal of respiratory cell and molecular biology* **59**, 511-522 (2018).
40. Gsell S, Loiseau E, D’Ortona U, Viallat A, Favier J. Hydrodynamic model of directional ciliary-beat organization in human airways. *Scientific Reports* **10**, 8405 (2020).
41. Khelloufi M-K*, et al.* Spatiotemporal organization of cilia drives multiscale mucus swirls in model human bronchial epithelium. *Scientific Reports* **8**, 2447 (2018).
42. Mitchell B, Stubbs JL, Huisman F, Taborek P, Yu C, Kintner C. The PCP Pathway Instructs the Planar Orientation of Ciliated Cells in the Xenopus Larval Skin. *Current Biology* **19**, 924-929 (2009).
43. Reiten I*, et al.* Motile-Cilia-Mediated Flow Improves Sensitivity and Temporal Resolution of Olfactory Computations. *Current Biology* **27**, 166-174 (2017).
44. Kermen F, Franco LM, Wyatt C, Yaksi E. Neural circuits mediating olfactory-driven behavior in fish. *Front Neural Circuits* **7**, 62 (2013).
45. Hansen A, Zeiske E. Development of the olfactory organ in the zebrafish, Brachydanio rerio. *Journal of Comparative Neurology* **333**, 289-300 (1993).
46. Pathak N, Austin-Tse CA, Liu Y, Vasilyev A, Drummond IA. Cytoplasmic carboxypeptidase 5 regulates tubulin glutamylation and zebrafish cilia formation and function. *Molecular biology of the cell* **25**, 1836-1844 (2014).
47. Nanjundappa R*, et al.* Regulation of cilia abundance in multiciliated cells. *Elife* **8**, e44039 (2019).
48. Klos Dehring Deborah A, Vladar Eszter K, Werner Michael E, Mitchell Jennifer W, Hwang P, Mitchell Brian J. Deuterosome-Mediated Centriole Biogenesis. *Developmental Cell* **27**, 103-112 (2013).
49. Kulkarni SS, Marquez J, Date PP, Ventrella R, Mitchell B, Khokha M. Mechanical stretch scales centriole number to apical area via Piezo1 in multiciliated cells. *Elife* **10**, (2021).
50. Redmond SA*, et al.* Development of Ependymal and Postnatal Neural Stem Cells and Their Origin from a Common Embryonic Progenitor. *Cell Rep* **27**, 429-441.e423 (2019).
51. Shi D*, et al.* Celsr1 is required for the generation of polarity at multiple levels of the mouse oviduct. *Development* **141**, 4558-4568 (2014).
52. Engel AK, Fries P, Singer W. Dynamic predictions: Oscillations and synchrony in top–down processing. *Nature Reviews Neuroscience* **2**, 704-716 (2001).
53. Carter G, Knapp C, Nuttall A. Estimation of the magnitude-squared coherence function via overlapped fast Fourier transform processing. *IEEE Transactions on Audio and Electroacoustics* **21**, 337-344 (1973).
54. Diaz Verdugo C*, et al.* Glia-neuron interactions underlie state transitions to generalized seizures. *Nat Commun* **10**, 3830 (2019).
55. Gheber L, Korngreen A, Priel Z. Effect of viscosity on metachrony in mucus propelling cilia. *Cell Motility* **39**, 9-20 (1998).
56. Brokaw CJ. Effects of Increased Viscosity

on the Move Ments of Some Invertebrate Spermatozoa. *Journal of Experimental Biology* **45**, 113-139 (1966).
57. Katoh TA*, et al.* Three-dimensional tracking of microbeads attached to the tip of single isolated tracheal cilia beating under external load. *Scientific reports* **8**, 15562-15562 (2018).
58. Goldstein RE, Lauga E, Pesci AI, Proctor MRE. Elastohydrodynamic Synchronization of Adjacent Beating Flagella. *Phys Rev Fluids* **1**, (2016).
59. Gray J. The mechanism of ciliary movement. *Proceedings of the Royal Society of London Series B, Containing Papers of a Biological Character* **93**, 104-121 (1922).
60. Brumley DR, Polin M, Pedley TJ, Goldstein RE. Metachronal waves in the flagellar beating of Volvox and their hydrodynamic origin. *J R Soc Interface* **12**, 20141358 (2015).
61. Wan KY*, et al.* Reorganization of complex ciliary flows around regenerating Stentor coeruleus. *Philosophical Transactions of the Royal Society B* **375**, 20190167 (2020).
62. Ovadyahu D, Priel Z. Characterization of metachronal wave in beating cilia: distribution of phases in space. *Biorheology* **26**, 677-685 (1989).
63. Nawroth JC*, et al.* Motile cilia create fluid-mechanical microhabitats for the active recruitment of the host microbiome. *Proceedings of the National Academy of Sciences* **114**, 9510-9516 (2017).
64. Vladar EK, Bayly RD, Sangoram AM, Scott MP, Axelrod JD. Microtubules enable the planar cell polarity of airway cilia. *Current Biology* **22**, 2203-2212 (2012).
65. Wallingford JB, Mitchell B. Strange as it may seem: the many links between Wnt signaling, planar cell polarity, and cilia. *Genes & development* **25**, 201-213 (2011).
66. Clare DK*, et al.* Basal foot MTOC organizes pillar MTs required for coordination of beating cilia. *Nature Communications* **5**, 4888 (2014).
67. Bottier M, Thomas KA, Dutcher SK, Bayly PV. How Does Cilium Length Affect Beating? *Biophysical Journal* **116**, 1292-1304 (2019).
68. Pintado P, Sampaio P, Tavares B, Montenegro-Johnson TD, Smith DJ, Lopes SS. Dynamics of cilia length in left–right development. *Royal Society Open Science* **4**, 161102 (2017).
69. Pikovsky A, Kurths J, Rosenblum M, Kurths J. *Synchronization: a universal concept in nonlinear sciences*. Cambridge university press (2003).
70. Feriani L*, et al.* Assessing the Collective Dynamics of Motile Cilia in Cultures of Human Airway Cells by Multiscale DDM. *Biophysical Journal* **113**, 109-119 (2017).
71. Gheber L, Priel Z. Synchronization between beating cilia. *Biophys J* **55**, 183-191 (1989).
72. Caron A, Xu X, Lin X. Wnt/β-catenin signaling directly regulates Foxj1 expression and ciliogenesis in zebrafish Kupffer's vesicle. *Development* **139**, 514-524 (2012).
73. Schindelin J*, et al.* Fiji: an open-source platform for biological-image analysis. *Nature methods* **9**, 676-682 (2012).
74. Vladimirov N*, et al.* Light-sheet functional imaging in fictively behaving zebrafish. *Nat Methods* **11**, 883-884 (2014).
75. Bartoszek EM, Jetti SK, Chau KTP, Yaksi E. Ongoing habenular activity is driven by forebrain networks and modulated by olfactory stimuli. *bioRxiv*, 2021.2002.2014.431141 (2021).
76. Jetti SK, Vendrell-Llopis N, Yaksi E. Spontaneous activity governs olfactory representations in spatially organized habenular microcircuits. *Curr Biol* **24**, 434-439 (2014).
77. Bean G. hexscatter.m.). MATLAB Central File Exchange (2021).
78. Bogovic JA, Hanslovsky P, Wong A, Saalfeld S. Robust registration of calcium images by learned contrast synthesis. In: *2016 IEEE 13th International Symposium on Biomedical Imaging (ISBI)*) (2016).
79. Asakawa K*, et al.* Genetic dissection of neural circuits by Tol2 transposon-mediated Gal4 gene and enhancer trapping in zebrafish. *Proc Natl Acad Sci U S A* **105**, 1255-1260 (2008).
80. Pan YA*, et al.* Zebrabow: multispectral cell labeling for cell tracing and lineage analysis in zebrafish. *Development (Cambridge, England)* **140**, 2835-2846 (2013).

METHODS

Experimental model and subject details

The animal facilities and maintenance of the zebrafish, *Danio rerio*, were approved by the NFSA (Norwegian Food Safety Authority). Fish were kept in 3,5L tanks in a Techniplast Zebtech Multilinking system at constant conditions: 28°C, pH7 and 600µSiemens, at a 14:10 hour light/dark cycle to simulate optimal natural breeding conditions. Fish were fed twice a day with dry food (ZEBRAFEED; SPAROS I&D Nutrition in Aquaculture), and once with *Artemia nauplii* (Grade0, platinum Label, Argent Laboratories, Redmond, USA). Larvae were maintained in egg water (1.2 g marine salt and 0.1% methylene blue in 20 L RO water) from fertilization to 3 dpf and subsequently in AFW (1.2g marine salt in 20L RO water). For experiments, the following fish lines were used: *hspGGFF19B;UAS:GFP* [43]. *Foxj1a:GCaMP6s* transgenic animals were generated in our laboratory upon co-injection of tol2 transposase mRNA and pCS2-Foxj1a:GCaMP6s plasmid containing the 0.6kb Foxj1a promoter described in upstream of GCamp6s open reading frame[72]. Experiments were performed on embryos of AB Background. All procedures were performed on zebrafish larvae at 4 dpf in accordance with the directive 2010/63/EU of the European Parliament and the Council of the European Union and the Norwegian Food Safety Authorities.

Immunohistochemistry

Euthanized larvae were fixed in a solution containing 4% paraformaldehyde solution (PFA), 0.3% Triton X-100 in PBS (0.3% PBSTx) for at least 3 hr at room temperature. Larvae were washed with 0.3% PBSTx (3x5 min) and permeabilized with acetone (100% acetone, 10 min incubation at −20°C). Subsequently, samples were washed with 0.3% PBSTx (3x10 min) and blocked in 0.1% BSA/0.3% PBSTx for 2 hr. Larvae were incubated with glutamylated tubulin (GT335, 1:400, Adipogen), and beta-catenin (#9562, 1:200, Cell Signalling Technologies) or gamma-tubulin (GTU-88, 1:400, Abcam) overnight at 4°C. On the second day samples were washed (0.3% PBSTx, 3x1 hr) and subsequently incubated with the secondary antibody (Alexa-labelled GAM555 plus, Thermo Scientific, 1:1,000) overnight at 4°C. The third day samples were incubated with 0.1% DAPI in 0.3% PBSTx, Life Technology, 2 hr), washed (0.3% PBSTx, 3x1 hr) and transferred to a series of increasing glycerol concentrations (25%, 50% and 75%). Stained larvae were stored in 75% glycerol at 4°C and imaged using a Zeiss Examiner Z1 confocal microscope with a 20x plan NA 0.8 objective. An antibody against GFP (Millipore, ab16901, and Alexa488-anti-chicken, Thermo Scientific) was used to enhance the GFP signal if needed. Acquired images were processed with Fiji/ImageJ [73]. Numbers of cells were counted using the "Cell Counter" plugin for Fiji/ImageJ (Kurt De Vos, Univ Sheffield, Academic Neurology, https://imagej.nih.gov/ij/plugins/cell-counter.html). The apical surfaces were collected from the beta-catenin staining using Fiji. The ciliary length was measured from cilia in their extended shape in the *hspGGFF19B;UAS:GFP* line using Fiji. The number of cilia was acquired from the gamma-tubulin staining, at 40X. Using Fiji, first an ROI was drawn around the apical surface of a cell. The crop was then rescaled and applied with an FFT bandpass filter (up to 50px; down to 6px; Suppress stripes: None; Tolerance of direction: 50%), and finally used the detect peaks function in Fiji (prominence = 50). Ciliary direction was identified per cell by comparing the relative position of gamma tubulin compared to glutamylated tubulin, imaged at both 20X and 40X. All measurements were further processed in Matlab.

Light transmission recordings

High-speed microscopy recordings of motile cilia were conducted with 4 days old larvae paralyzed with an intramuscular injection of α-bungarotoxin (Invitrogen BI601, 1 mg/mL and then embedded in 0.75% low melting point agarose prepared in AFW in a FluoroDish (World Precision Instruments). Specifically, animals were mounted carefully at a 15degree angle and titled to one side, fully exposing the lateral region of the nose. Agarose covering the nostrils was removed to allow free ciliary beating. The mounted fish was left to rest for five minutes to properly set the agarose and avoid drift. Olfactory pits of zebrafish larvae were visualized by a Bresser transmitted light microscope using a 63x water immersion objective lens (Zeiss, NA 0.9, plan). The microscope was stabilized using Sorbothane feet blocks (Thorlabs; AV4 - Ø27.0 mm). High-speed digital recordings were captured with an Allied Vision Manta camera (G-031B) at 99-110 frames per second (Fs) at a resolution of 0.15µm/pixel. Frames were acquired and stored by custom made software written in C++, and further analysis was conducted in MATLAB (Mathworks).

Light sheet recordings

h*spGGFF19B;UAS:GFP* larvae were imaged using a custom-build light-sheet microscope (based on the design described by [74]) with a 20x water immersion objective (Olympus, NA 1.00, plan), a 4X illumination objective (Olympus, NA 0.28, XLFLUOR-340), a Hamamatsu CMOS camera (C11440-42U30), PXI system for instrument control (NI PXI 1042Q), and a laser of 488 nm wavelength (Cobolt). Multiciliated cells in the zebrafish nose were recorded for 1-2 sec at 300-500Hz. Paralyzed larvae were mounted in 1.5% Low melting point agarose, agarose was removed in front of their nose, and larvae were positioned in a custom-build

chamber so that the multiciliated cells directly faced the light sheet. Images were acquired by the Zebrascope software in LabView [74] and analysed in ImageJ/Fiji and MATLAB. The light-sheet was adapted to allow for sequential light transmission image acquisition using the same Zebrascope software. Sequential imaging in light-sheet and light transmission mode of h*spGGFF19B;UAS:GFP* animals (4dpf), sparsely labelling multiciliated cells in the nose, to compare the contribution of ciliary beating of one cell to the entire ciliated epithelium. In addition, the light transmission mode was used to acquire sequential ciliary beat recordings with 10µm spacing (100Hz), effectively creating a 3D ciliary beating map of the zebrafish nose.

Viscosity experiments

Methylcellulose 15cP (M7140-100G; Sigma-Aldrich) was dissolved at 2% (w/v) in Artificial Fish Water (AFW) overnight (500rpm). Serial dilutions were performed to achieve lower concentrations of methylcellulose in AFW (0.25%, 0.5%, 1%, and 2%), corresponding to (1,875cP; 3.75cP; 7.5cP; 15cP). Using light transmission microscopy as described above, a 60s baseline was first recorded at 100Hz in AFW, after which AFW was exchanged for a viscous solution. After settling for five minutes, the nose is recorded again for 60s. This was repeated until the fish were recorded with all increasing concentrations and a return to baseline AFW. In another set of experiments, light-sheet experiments were performed as described above. A 4s baseline was first recorded at 500Hz in AFW, after which AFW was exchanged for increasingly more viscous solutions. After settling for five minutes, the nose is recorded again for 4s. Data were further analyzed for CBF, using the framework described above, and ciliary waveforms in Fiji.

Analysis pipeline for wave direction and wavelength

Beating cilia interfere with the transmission of light and result in an oscillatory change of light intensity over time [14]. We established an analysis pipeline based on the analysis in [43].

All codes including the dataset represented in Figure 4B-F is published on Mendeley Data with the following DOI 10.17632/th35c5833g.1.

Frequency

We analyzed the frequency of oscillations for every pixel of the recording by computing the Fourier transform of the corresponding intensity time series of that pixel using the Matlab fast Fourier transform (*fft()*). To increase computational speed, we spatially down-sampled each frame by a factor 5. For each pixel, cilia beat frequency (CBF) was calculated as the frequency (between 15 Hz and half the frequency of acquisition) where the absolute value of the Fourier transform was maximal. This resulted in a spatial CBF map. As beating cilia do not cover the entire recording area, we automatically segmented this area into signal and noise pixels, using a threshold for the local standard deviation (SD). In brief, we moved a 3x3 kernel across the entire frequency map and any pixel belonging to a 3x3 kernel whose SD was below 3Hz was considered as signal, whereas pixels belonging only to kernels with an SD above 3Hz were considered as noise. To remove small signal regions, we listed all connected pixels in the frequency map using the *bwconncomp()* Matlab function, and removed regions with fewer than 500 pixels. Altogether, with SD-thresholding and by removing small signal regions, we robustly identified those regions of the imaging area with beating cilia.

Coherence and coherence-versus-distance calculations

The coherence score constitutes a normalized cross-power spectral density: for a pair of time series $x(t)$ and $y(t)$, it is defined as

(1)
$$C_{xy}(f) = \frac{|P_{xy}(f)|^2}{P_{xx}(f)P_{yy}(f)},$$

where

- $C_{xy}(f)$ is the magnitude-squared coherence score of the two time series $x(t)$ and $y(t)$ as function of frequency f
- $P_{xy}(f)$ is the cross-power spectral density of $x(t)$ and $y(t)$
- $P_{xx}(f)$ and $P_{yy}(f)$ are the power spectral densities of $x(t)$ and $y(t)$, respectively.

One may think of $P_{xx}(f)$ and $P_{yy}(f)$ as the squared magnitude of the Fourier transforms of $x(t)$ and $y(t)$, whereas $P_{xy}(f) \sim x^*(f)\, y(f)$ is related to the product of the Fourier transforms of $x(t)$ and $y(t)$.

We apply the coherence score to the intensity time series $x(t)$ and $y(t)$ corresponding to a pair of signal pixels. Figure 2D shows an example of input time series and resulting coherence score, see top and bottom panels.

Specifically, coherence scores were calculated for 30 s long raw recordings (approx. 99-110 frames per second; parameter: Fs) using an adapted version of the Matlab *mscohere()* built-in function. In short, *mscohere()* takes two signals and returns the coherence as a function of frequency with values between 0 and 1 ($C_{xy}(f)$). In detail, we first calculated the power spectra for the two time series $x(t)$ and $y(t)$ ($Pxx(f)$) and

Pyy(f)) using Welch's method with parameters *pwelch(Pxx, window, noverlap, nfft, Fs, 'psd').* Second, we calculated the cross spectrum for the *x(t)* and *y(t)*, *(Pxy(f))* using the Matlab function *cpsd(Pxx, Pyy, window, noverlap, nfft, Fs)* with parameters window = *hamming(*100*)*; noverlap = 80; nfft = 100. Finally, we estimated a dimensionless coherence score from the power spectra and cross spectrum according to Eq. (1).
To evaluate coherence in space, we either calculated the coherence for one reference pixel with all other pixels, or for all pixel-pairs in the recording. We use the latter pixel-pairs to plot coherence-*versus*- distance, a measure similar to the correlation-*versus*-distance analysis employed by previous authors [75, 76]. Since *mscohere()* recalculates the power spectra for a given pixel each time coherence is estimated, we reduced the computing costs by retaining the power spectra. In addition, when calculating the coherence for all pixel-pairs, we spatially down-sampled each frame by a factor 5 and discarded all pixels outside the signal region. In the end, to visualize the coherence-*versus*-power, and coherence-*versus*-distance measured, we plotted the density using *hexscatter()*[77], using distance bins of width 0.5 µm and bins of width 0.04 for the coherence.

Segmentation
To segment the frequency map into distinct frequency patches, we first bin the power spectra into 100 bins (~ 0.5Hz). We then divide the map into frequency patches by grouping same frequency pixels using *bwconncomp()* with two-dimensional eight-connected neighborhood as the desired connectivity, and finally set a minimum size for a patch to 200 pixels. These frequency patches underlie the further analysis.
Phase
Phase, or phase angle, was extracted from the complex Fourier output by taking the *angle()*. But instead of taking a pixel-based approach, we took a patch-based approach: for all pixels of a given patch, we extracted the phase angle at the main frequency of that patch.
Gradients
From the segmented phase angle maps, we generated gradient maps by computing the image gradient *imgradientxy(phase, 'prewitt')* over both x and y direction, as well as over phase and phase+ π to adjust for the circular nature of the phase. From these gradient maps, wave directions are extracted by taking the mean angle per patch, while wavelengths are extracted by taking the mode magnitude per patch.
Detection of ciliary direction and rotating using BigWarp
To compare the noses of different fish, we aligned raw recording frames using BigWarp [78]. We choose to perform the *rotation* morphometric transformation. The raw recordings were preselected based on their anatomy: we found that fish exposing much of the lateral region of the nose, tend to have a stronger and larger signal. All animals were aligned to a reference fish left nose (Fig. 4). Upon aligning the recordings based on spatial features such as, pit edges, centre, and skin regions, we extracted the landmarks before and after the transformation. In addition, all right noses were flipped vertically preceding the transformation. Finally, we applied the transformations, associated with the imported landmarks, to the outputs of the analysis pipeline: frequency, phase, wave direction and wavelength maps.

Computational model
We consider a computational model of a cilia carpet, where cilia are regularly spaced on a triangular lattice (lattice spacing 18 mm) with aligned cilia polarity, see [27] for details. Specifically, we employed a unit cell of 16x16 cilia, for which periodic boundary conditions are imposed. This defines a finite set of possible perfect traveling waves of cilia phase compatible with the boundary conditions, each characterized by different wave direction angle q and wavelength l, see Fig. 6A. Insets visualize example waves, where the color of dots at respective cilia positions encodes cilia phase. Python packages are available on github to (i) reconstruct 3D curves from orthogonal 2D projections: https://github.com/icemtel/reconstruct3d_opt , (ii) create triangulated surface meshes and solve hydrodynamic Stokes equation: https://github.com/icemtel/stokes, and (iii) study systems of coupled oscillators https://github.com/icemtel/carpet .

Cilia pumping rate
We computed the mean pumping rate per cilium for different wave solutions as follows: Detailed hydrodynamic computations based on a triangulated surface mesh for a set of neighboring cilia and the boundary surface were conducted using the Stokes equation valid at low Reynolds numbers as detailed in [27]. The three-dimensional cilia beat pattern used had been previously tracked from *Paramecium* using stereographic recordings [16]. Due to the linearity of the Stokes equation, the individual contributions of all cilia add up and it is sufficient to consider a scenario, where only a single cilium, say at position $\mathbf{x}_j$ and phase f_j, moves with phase speed $d\phi_j/dt$, while all other cilia at positions $\mathbf{x}_i$ remain immotile with fixed phase ϕ_i. Detailed hydrodynamic computations then yielded a surface distribution $\phi(\mathbf{x})$ of hydrodynamic friction forces, which depends on the vector of cilia phases and is linear in the phase speed $d\phi_j/dt$. Exploiting once more the linearity of the Stokes

equation, the instantaneous pumping rate $\mathbf{Q}_j$ of the central cilium can be computed as a surface integral of all local contributions to fluid pumping arising from this force density over the surface S of all cilia: the pumping due to a point-force of magnitude $\mathbf{F}$ coplanar with a planar no-slip boundary at height z above the surface is given by $\mathbf{F}\, z / \pi\eta$, where h is the dynamic viscosity of the fluid [24]. This result was found by integrating Blake's fundamental solution for the flow field induced by a point force near a no-slip boundary; up to prefactor, this result follows also from symmetry considerations and dimensional analysis. We thus find for the instantaneous pumping rate vector (with units of volume pumped per unit time)

$$\mathbf{Q}_j\,(\phi_1, \ldots, \phi_N) = (\pi\eta)^{-1} \int_S d^2\mathbf{x}\, \mathbf{f}(\mathbf{x})\, z.$$

To economize simulations, this surface integral can be split into contributions from integrating over the surface of different cilia as $\mathbf{Q}_j = \Sigma_i\, \mathbf{Q}_{ij}$. Importantly, here the contribution $\mathbf{Q}_{ij}$ stemming from integrating over the surface S_i of cilium i depends on the phase ϕ_j of the central cilium that is moving and the phase ϕ_i of non-moving cilium i, but is virtually independent of the phases of the other cilia, i.e., $\mathbf{Q}_{ij} \approx \mathbf{Q}_{ij}(\phi_i, \phi_j)$. Due to the linearity of the Stokes equation, each of these contributions is linear in the phase speed of the central cilium, $\mathbf{Q}_{ij}(\phi_i, \phi_j) = \mathbf{q}_{ij}(f_i, f_j)\, df_j/dt$ with pumping coefficient $\mathbf{q}_{ij}(\phi_i, \phi_j)$. This allows efficient tabulation of computation results for combinations of neighbors and pairs of cilia phases. Moreover, we confirmed that hydrodynamic interactions between distant cilia are weak and therefore only included the contributions from nearest and certain next-to-nearest neighbors (along the direction of the cilia effective stroke), for which hydrodynamic are strongest [27]. Generally, the contribution from the other cilia, $\mathbf{Q}_{ij}$ for $i \neq j$, points in the direction opposite of $\mathbf{Q}_{jj}$ (but is weaker in magnitude), because the other cilia act as obstacles for the fluid flow generated by the central cilium j. Finally, the instantaneous pumping rate vector $\mathbf{Q}_j\,(f_1, \ldots, f_N)$ was averaged over a full beat cycle and all cilia indices j, to yield a mean pumping rate vector $\mathbf{Q}$ per cilium.
Of note, in an infinite cilia carpet of density r, the mean pumping rate per cilium sets a slip velocity of approximately steady fluid flow $\boldsymbol{v}_{slip}$ at a suitable height above the cilia carpet as [24]

$$\mathbf{v}_{slip} = \pi\, \rho\, \mathbf{Q} = \mathbf{F}\, h / \eta\ .$$

We computed the pumping rate vector $\mathbf{Q}$ for different traveling waves, where the wave vector $\mathbf{k}$ of the waves determines the phase difference of neighboring cilia. The scalar magnitude $Q=|\mathbf{Q}|$ is reported for all possible $\mathbf{k}$ in Fig. 6B. There, the scalar pumping rates $Q(\mathbf{k})$ were normalized by the pumping rate $Q_{rand} = |\mathbf{Q}_{rand}|$ for cilia beating with random phase relationship. For the cilia density and beat pattern used, $\mathbf{Q}_{rand}$ / (μm^3/ms) ≈ 1.452 $\mathbf{e}_x$ + 7.739 $\mathbf{e}_y$, with unit vector $\mathbf{e}_y$ pointing in the direction of the effective stroke of the cilia beat. This pumping rate $\mathbf{Q}_{rand}$ used for normalization was determined by initializing cilia phases with random values (uniformly distributed in the interval $[0,2\pi]$), and integrating the dynamics of the cilia carpet over one full beat cycle (corresponding to the increase of the global phase by 2π); results were averaged over n=100 stochastic realizations.
The mean pumping rate vector $\mathbf{Q}$ is parallel to the boundary surface. We can thus report its direction angle relative to the direction of the effective stroke of the cilia beat, see Fig. 6C.

Impact of noise
To investigate the effect of imperfect synchronization, we performed dynamic simulations of the cilia carpet model from [27] with perturbed initial conditions and computed the mean pumping rate averaged over one beat cycle. Specifically, initial conditions were chosen as a perfect traveling wave as indicated, with independent normal distributed random numbers with variance σ^2 added to the initial phase of each cilium (as well as a global random phase offset uniformly distributed in the interval $[0,2\pi]$). The dynamics was then integrated for a full beat cycle, see Fig. 6D. For large values of s, the pumping rates converged to the rate Q_{rand} corresponding to cilia beating with random phase relationship. All results represent averages of n=100 independent realizations.

Critical density
The dilute spacing of cilia in the computational model prevents steric interactions between cilia. We determined for each possible wave solution with wave vector $\mathbf{k}$ the highest density $r_{\mathbf{k}}$ at which still no steric interactions occur at any point of the beat cycle (determined by a minimal distance of the respective centerlines of neighboring cilia of more than 0.5 μm) by down-scaling the lattice spacing of the triangular arrangement of cilia, see Fig. 6E. Analogously, we determined a similar critical density ρ_{rand} for cilia beating with random phase relationship, by testing all possible phase relationships of neighboring cilia.
We confirmed that results are robust: if for a pair of neighboring cilia instead of the exact value of the phase difference $\Delta\phi$ between their respective phases as determined by the wave solutions under consideration,

a phase difference from the interval $[\Delta\phi-\sigma,\Delta\phi+\sigma]$ is chosen, we obtain very similar results even for phase fluctuations with σ=0.4.